

The influence of van der Waals interactions on a bubble moving in a tube

NAIMA HAMMOUD¹, PHILIPPE H. TRINH²,
PETER D. HOWELL² AND HOWARD A. STONE³

¹ Program in Applied and Computational Mathematics,
Princeton University, Princeton, NJ 08544, USA

² Oxford Centre for Industrial and Applied Mathematics,
Mathematical Institute, University of Oxford, Oxford OX2 6GG, UK

³ Department of Mechanical and Aerospace Engineering,
Princeton University, Princeton, NJ 08544, USA

(Received 04 January 2016 [Draft])

We consider the unsteady thin-film dynamics of a long bubble of negligible viscosity that advances at a uniform speed in a cylindrical capillary tube. The bubble displaces a viscous non-wetting fluid, creating a thin film between its interface and the tube walls. The film is considered thin enough that intermolecular forces in the form of van der Waals attractions are significant and thin-film rupture is possible. In the absence of intermolecular forces, the bubble has a steady-state where a film of uniform thickness is deposited in the annular region between the bubble interface and the tube walls. However, once intermolecular forces are present, the bubble interface is perturbed out of its steady-state and either (i) the perturbation grows sufficiently before reaching the rear meniscus of the bubble such that rupture occurs; or (ii) the perturbation remains small due to weak intermolecular forces until it leaves the bubble interface through the rear meniscus. We obtain, both numerically and asymptotically, the time-scale over which rupture occurs. We thus find a critical capillary number, depending on the bubble length and the strength of the intermolecular forces, below which the film is predicted to rupture.

1. Introduction

When an air bubble advances in a circular tube filled with an immiscible wetting fluid, a uniform thin film is deposited between the bubble interface and the tube walls. This setup was first studied experimentally by Fairbrother & Stubbs (1935), and later, it was shown by Taylor (1961) that the speed of the bubble is higher than the average speed of the surrounding fluid; this is an indication that the thickness of the deposited film increases with increasing bubble speed. A theoretical framework using the lubrication approximation was proposed by Bretherton (1960), who found that the thickness of the uniform film varies as a two-thirds power law with the capillary number, measuring the relative strength of viscous to surface tension forces. Although this theoretical result was shown to be valid only in the limit of small capillary numbers, experiments were conducted by Bretherton to further verify the range of validity of this result.

Since Bretherton, there has been much work on the problem of an inviscid bubble moving in a tube, and displacing a viscous, wetting fluid [*c.f.* Goldsmith & Mason 1963; Schwartz *et al.* 1986; Wong *et al.* 1995*a,b*]. The bubble configuration was extended by Park & Homsy (1984), and then further developed by Hodges *et al.* (2004), to include the steady motion of an immiscible viscous drop, displacing a wetting viscous fluid. The case of a viscous drop displacing a non-wetting viscous fluid was first introduced by Teletzke

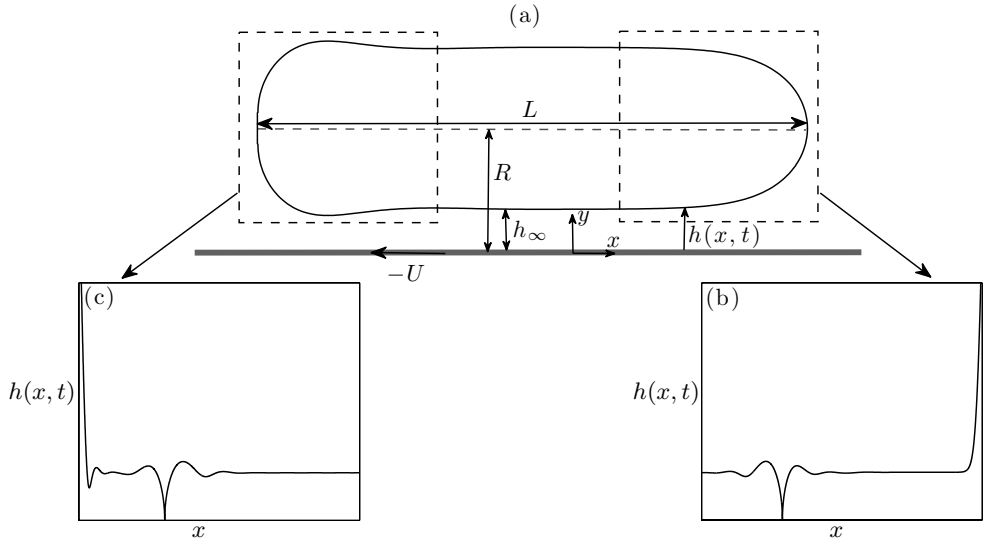


Figure 1: Bubble translating past a boundary. (a) Bubble interface with two domains highlighted: the front meniscus, and the rear meniscus of the bubble. (b) Rupture of the thin film as a perturbation advances away from the front meniscus. (c) Rupture of the thin film as a perturbation advances towards the rear meniscus.

et al. (1988), who showed numerically that there is a critical capillary number below which steady films of uniform thickness cannot be obtained due to rupture of the film. This result was qualitatively verified by the experiments of Chen *et al.* (2013). Other studies have extended the bubble in a tube problem to account for *e.g.* flexibility of the substrate, and this is an important effect in medical applications such as airway closure (Gaver *et al.* 1996; Heil 1999; Tai *et al.* 2011).

In this paper, we are interested in the particular situation of a non-wetting fluid surrounding the bubble or drop, where the presence of attractive intermolecular forces can be destabilising, and consequently, the thin film may rupture. In their experimental work, Chen *et al.* (2013) studied the dynamics of oil droplets advancing in a tube filled with water, where one region of the tube was made hydrophobic, while the other was kept hydrophilic. Rupture was observed in the hydrophobic region for slowly moving drops. However, once the drops were advanced at speeds larger than some critical value, it was observed that rupture was suppressed.

In order to find the conditions under which rupture suppression can occur, we study the above scenario theoretically and numerically. The bubble configuration is illustrated in Fig. 1(a), and the mathematical model is developed in Sec. 2.1. The subfigures 1(b) and 1(c) show two instances where rupture has occurred near the front or the rear meniscus of the bubble. The surface profiles are plotted from time-dependent numerical simulations of the front and rear menisci. Here, they are shown without scale only so as to illustrate the qualitative phenomena of rupture; see Hammoud (2016) and Sec. 3 for more details on the numerical implementation.

Note that rupture, or adhesion, is not always a desired phenomenon, especially in applications that involve self-cleaning surfaces (Roach *et al.* 2008; Koch *et al.* 2009; Erbil *et al.* 2003). However, in some circumstances, rupture can be beneficial, such as in targeted drug delivery (Arap *et al.* 1998), or by using the adhesive properties of tumor cells to promote separation from healthy cells (Blackstone *et al.* 2012). The theoretical

approach to thin-film rupture is typically developed in the framework of slow viscous flow (lubrication) theory, by the addition of attractive intermolecular forces, such as van der Waals attractions (Burelbach *et al.* 1988; Ida & Miksis 1996; Witelski & Bernoff 2000). Self-similar analyses have been provided of rupturing film profiles (Zhang & Lister 1999; Witelski & Bernoff 1999). Also, studies have been reported of rupture delay by adding surfactants or increasing the flexibility of the substrate supporting the rupturing film (Matar & Kumar 2004), and of rupture suppression by adding an external shear to the thin film (Kalpathy *et al.* 2010; Davis *et al.* 2010).

We begin this study in Sec. 2.1 by using lubrication theory to derive the thin-film equation that governs the bubble dynamics when attractive van der Waals interactions are present. In Secs. 2.2 and 2.3, we study the steady-state profiles of the shape of the bubble as a function of a non-dimensional van der Waals parameter, β , that characterises the strength of the intermolecular forces. Asymptotics are developed for large and small values of β , and a relation between film thickness and capillary number is found. Unsteady dynamics are studied in two ways: first, a linear stability analysis is performed in 3.2; second, in Secs. 3.3–3.5, we study the effect of a sudden transition as the interface moves from a wetting to a non-wetting region in the tube. In Sec. 3.6, this analysis is shown to yield a critical capillary number beyond which rupture is predicted to be suppressed.

2. Theory

2.1. Mathematical model

We consider an inviscid, long bubble moving at a constant speed U through a capillary tube of radius R , which is filled with a non-wetting viscous fluid of viscosity μ and density ρ . The bubble is assumed to be at least a few tube radii long. The motion of the bubble displaces the viscous fluid, which causes the deposition of a uniform thin film in the annular region between the bubble interface and the tube walls (see Fig. 1(a)). The interfacial tension between the displaced fluid and the bubble is denoted by γ . The deposited film has a thickness h_∞ , and is considered thin enough that intermolecular forces in the form of long range destabilising van der Waals attractions are significant.

In the limit that the film thickness is very small compared to the tube radius, the system can be characterised locally as two-dimensional. Thus, we use Cartesian coordinates (x, y) and time t to represent the spatial and temporal dynamics. The x -coordinate describes lateral positions of the bubble in the tube. We treat the front and rear menisci of the bubble separately. When treating the front meniscus of the bubble, we refer to $x \rightarrow \infty$ as the front bubble cap, $x \rightarrow -\infty$ as the uniform thin film of thickness h_∞ . When treating the rear meniscus, we refer to $x \rightarrow -\infty$ as the rear bubble cap, $x \rightarrow \infty$ as the uniform thin film of thickness h_∞ .

Following Bretherton (1960), we assume that both the Weber number, $\rho RU^2/\gamma$, and the Bond number, $\rho g R^2/\gamma$, are very small, and we therefore neglect both inertial and gravitational effects. The thickness of the film from the tube wall, i.e. $y = 0$, to the bubble interface is denoted by $h(x, t)$, and in the limit that $|\partial h/\partial x|$ is small, we can use the lubrication approximation to derive the equation describing thin-film dynamics.

Given these assumptions, the momentum equation in the absence of inertial and gravitational effects reduces to

$$\frac{\partial p}{\partial x} = \mu \frac{\partial^2 u}{\partial y^2} \quad \text{and} \quad \frac{\partial p}{\partial y} = 0, \quad (2.1)$$

where $u(x, y)$ is the x -component velocity profile of the displaced fluid in the region

between the bubble interface and the tube walls. The pressure is given by

$$p = -\gamma \frac{\partial^2 h}{\partial x^2} + \frac{A}{6\pi h^3}, \quad (2.2)$$

which is a combination of the capillary pressure, $-\gamma \partial^2 h / \partial x^2$, and the disjoining pressure due to attractive van der Waals intermolecular forces, $A/6\pi h^3$, with A being the Hamaker constant discussed below. It is convenient to work in the reference frame of the bubble, in which case the fluid is subject to a no-slip boundary condition on the solid substrate, and a zero shear condition at the free surface:

$$u(x, 0) = -U \quad \text{and} \quad \left. \frac{\partial u}{\partial y} \right|_{y=h} = 0. \quad (2.3)$$

The velocity u is found by integrating (2.1) subject to the boundary conditions given in (2.3), and using (2.2). The depth-averaged flux, q , is then given by

$$q = \int_0^h u \, dy = \frac{1}{3\mu} \left[\gamma h^3 \frac{\partial^3 h}{\partial x^3} + \frac{A}{2\pi h} \frac{\partial h}{\partial x} \right] - Uh. \quad (2.4)$$

Mass conservation then leads to the equation describing the thin-film dynamics (Oron *et al.* 1997)

$$\frac{\partial h}{\partial t} + \frac{1}{3\mu} \frac{\partial}{\partial x} \left[\gamma h^3 \frac{\partial^3 h}{\partial x^3} + \frac{A}{2\pi h} \frac{\partial h}{\partial x} \right] - U \frac{\partial h}{\partial x} = 0. \quad (2.5)$$

We non-dimensionalise (2.5) using the dimensionless variables H , X , and T , such that

$$H = \frac{h}{h_\infty}, \quad X = \frac{x}{h_\infty \text{Ca}^{-1/3}}, \quad T = \frac{t}{h_\infty \text{Ca}^{-1/3}/U}, \quad (2.6)$$

where $\text{Ca} = 3\mu U / \gamma$ is the capillary number. Equation (2.5) in dimensionless form reads

$$\frac{\partial H}{\partial T} + \frac{\partial}{\partial X} \left[H^3 \frac{\partial^3 H}{\partial X^3} + \frac{\beta}{H} \frac{\partial H}{\partial X} \right] - \frac{\partial H}{\partial X} = 0, \quad (2.7)$$

where we have introduced the dimensionless van der Waals parameter,

$$\beta = \frac{A}{2\pi\gamma h_\infty^2 \text{Ca}^{2/3}}. \quad (2.8)$$

Note that when $\beta < 0$, i.e. $A < 0$, the intermolecular forces are repulsive, hence stabilising, and the displaced fluid wets the substrate (Chaudhury *et al.* 2014). On the other hand, when $\beta > 0$, i.e. $A > 0$, these forces are attractive, thus, the displaced fluid is non-wetting, and may therefore cause instabilities that lead to rupture of the thin film.

In the absence of intermolecular forces, i.e. when $A = 0$, the translation of an inviscid bubble in a tube was analysed theoretically by Bretherton (1960). One of Bretherton's principal results was to show that the uniform film of thickness, h_∞ , deposited between the bubble interface and the tube walls varies with the capillary number as

$$\frac{h_\infty}{R} \sim \kappa_0 \text{Ca}^{2/3}, \quad (2.9)$$

where $\kappa_0 \approx 0.643$ is a numerically-determined constant.

In this work, we are interested in scenarios that may lead to rupture. Therefore, we consider the motion of a bubble surrounded by a non-wetting fluid in a tube, with $A > 0$

BOUNDARY CONDITIONS	FRONT MENISCUS	REAR MENISCUS
(a) $H = 1$	$X \rightarrow -\infty$	$X \rightarrow +\infty$
(b) $\partial H / \partial X = 0$	$X \rightarrow -\infty$	$X \rightarrow +\infty$
(c) $H = H_s(X; \beta)$	$X \rightarrow +\infty$	$X \rightarrow -\infty$
(d) $\partial^2 H / \partial X^2 = \kappa(\beta)$	$X \rightarrow +\infty$	$X \rightarrow -\infty$

Table 1: Boundary conditions for Eq. (2.7) for the front and rear menisci (Fig. 1(a) shows the coordinate system used).

$(\beta > 0)$. We solve (2.7) subject to one initial condition

$$H(X, 0; \beta) = H_s(X; \beta), \quad (2.10)$$

and four boundary conditions, shown in Table 1, which are satisfied by the film at the front and rear menisci. In (2.10), $H_s(X; \beta)$ is an initial profile that describes the shape of either the front or the rear meniscus of the bubble at steady state. We will assume that the film profile, $H(X, T; \beta)$, is quasi-static near the front (rear) of the bubble, as expressed in the boundary condition in Table 1(c). Also, $\kappa(\beta)$ corresponds to the linearised curvature of the meniscus of the bubble, where $\kappa(\beta) = \lim_{X \rightarrow +\infty} d^2 H_s / dX^2|_{\text{front}} = \lim_{X \rightarrow -\infty} d^2 H_s / dX^2|_{\text{rear}}$. By reversing the non-dimensionalisation (2.6), we see that $\kappa(\beta)$ is related to the uniform film thickness h_∞ in the bubble by

$$\frac{h_\infty}{R} = \kappa(\beta) \text{Ca}^{2/3}. \quad (2.11)$$

The profile for $H_s(X; \beta)$ will be determined below by first finding the steady-state solution of (2.7).

2.2. Steady-state solution

At steady-state, the film does not vary with time, i.e. $\partial H / \partial T = 0$. Thus, integrating (2.7) once with respect to X , and using the boundary conditions in Table 1(a) and 1(b) yields

$$H_s^3 H_s''' + \beta \frac{H_s'}{H_s} - H_s = -1, \quad (2.12)$$

where $H_s(X; \beta)$ is the steady-state profile of the thin film. Here, we use primes to denote differentiation with respect to the function argument, X . The above equation (2.12) is third order in X , and hence subject to three boundary conditions, shown in Table 2. As above, $\kappa(\beta)$ is the normalised curvature of the meniscus of the bubble, which varies as a function of the van der Waals parameter, β . Equation (2.11) implies that the value of κ at the rear meniscus must equal that at the front meniscus.

To find the steady-state profile for either the front or the rear meniscus, we start by perturbing the dimensionless film, $H_s(X; \beta)$, about the uniform film of unit thickness, i.e.

$$H_s(X; \beta) = 1 + \eta(X; \beta), \quad (2.13)$$

where $|\eta| \ll 1$. Using the ansatz (2.13), we linearise (2.12) to find

$$\eta''' + \beta \eta' - \eta = 0. \quad (2.14)$$

This equation has solutions of the form e^{mX} , where m is a root of the cubic equation $m^3 + \beta m - 1 = 0$. For $\beta > 0$, this cubic equation has one positive real root, m_1 , and two complex conjugate roots, m_2 and m_2^* , with negative real part, where $*$ denotes complex conjugation.

BOUNDARY CONDITIONS	FRONT MENISCUS	REAR MENISCUS
(a) $H_s = 1$	$X \rightarrow -\infty$	$X \rightarrow +\infty$
(b) $H'_s = 0$	$X \rightarrow -\infty$	$X \rightarrow +\infty$
(c) $H''_s = \kappa(\beta)$	$X \rightarrow +\infty$	$X \rightarrow -\infty$

Table 2: Boundary conditions for Eq. (2.12) for the front and rear menisci.

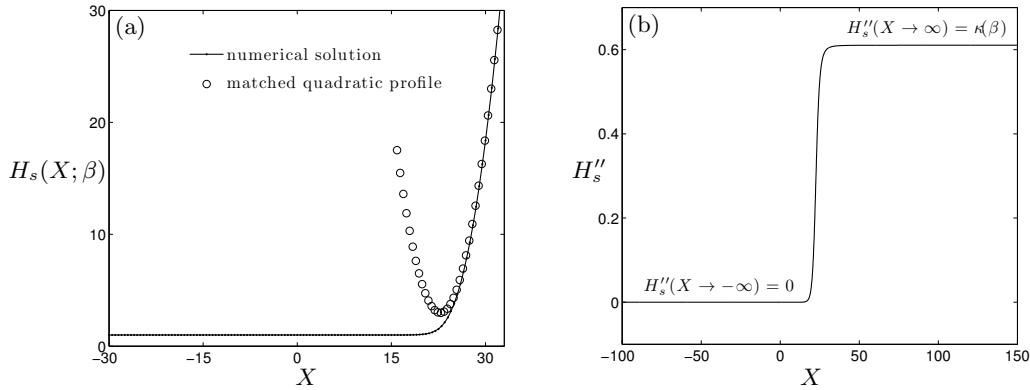


Figure 2: (a) Steady-state solution for a front bubble meniscus subject to attractive van der Waals forces for the case of $\beta = 0.2$. The circles correspond to a quadratic profile that matches the shape of the front meniscus of the bubble. (b) Variation in curvature of the bubble profile as a function of position. The curvature tends to a non-zero constant value $\kappa(\beta)$ for large positive X . For the case of $\beta = 0.2$, we find that $\kappa(0.2) \approx 0.611$.

We first find the steady-state profile of the front meniscus. In order to satisfy the boundary conditions in Table 2(a) and 2(b) at the front, the modes corresponding to the roots m_2 and m_2^* must equal zero. Thus, the solution asymptotes to a uniform film as

$$H_s(X; \beta)|_{\text{front}} = 1 + \eta_0 e^{m_1 X} \quad \text{as } X \rightarrow -\infty, \quad (2.15)$$

where η_0 is an integration constant, which may be set to 1 without loss of generality by exploiting translation invariance.

The solution for the front meniscus of the bubble is found by solving equation (2.12) subject to the far-field behavior (2.15). A typical profile for the front meniscus is shown in Fig. 2(a) for $\beta = 0.2$, and the corresponding profile for the curvature at different positions is provided in Fig. 2(b). For each value of β , the front meniscus of the bubble asymptotes to a unique quadratic profile with a constant curvature, $\kappa(\beta)$, as summarised in Fig. 3.

Having found the variation of the normalised curvature, $\kappa(\beta)$, with β , as well as the steady-state profiles of the front meniscus of the bubble (e.g. Fig 2(a)), we now switch to finding the steady-state profiles of the rear meniscus. To satisfy the boundary conditions in Table 2(a) and 2(b) for the rear meniscus of the bubble, the eigenfunction corresponding to m_1 must equal zero. Therefore, the rear meniscus asymptotes to a uniform film as

$$H_s(X; \beta)|_{\text{rear}} = 1 + \tilde{\eta}_0 e^{\Re(m_2)X} \cos(\Im(m_2)X + \phi) \quad \text{as } X \rightarrow +\infty, \quad (2.16)$$

the oscillations corresponding to capillary ripples at the rear cap of the bubble (Bretherton 1960; Wilson & Jones 1983). Here, $\tilde{\eta}_0$ and ϕ are integration constants, and again $\tilde{\eta}_0$ may be set to 1 without loss of generality. Therefore, we use $\phi \in [-\pi, \pi]$ as a shooting parameter,

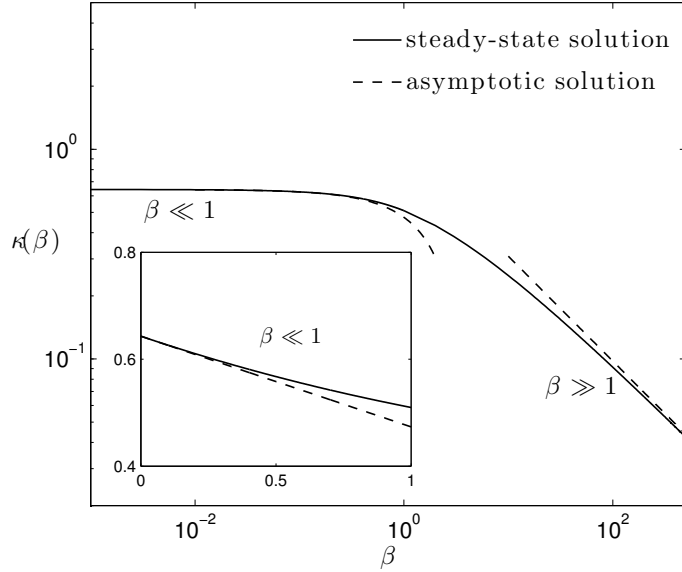


Figure 3: Numerically calculated curvature of the front meniscus of the bubble as a function of the dimensionless van der Waals interaction parameter, β (shown solid). The asymptotic predictions (shown dashed) in the small and large β limits, given by (2.19) and (2.25), closely match the numerical solutions. Inset: The curvature as a function of β , on a linear scale, for $\beta \ll 1$.

and find the value ϕ^* of ϕ such that the curvature of the rear meniscus of the bubble is equal to that of the front, $\kappa(\beta)$. In Fig. 4(a) we show a set of steady-state profiles of the rear meniscus of the bubble for $\beta = 0.2$, and a number of phase angles, ϕ . The bold dashed line of Fig. 4(a) corresponds to the profile that has a curvature equal to that of the front meniscus of the bubble. The convergence of the curvature of the rear meniscus to that of the front is plotted in Fig. 4(b).

2.3. Asymptotic behavior of $\kappa(\beta)$

When $\beta = 0$, Bretherton (1960) showed that h_∞/R increases with $\text{Ca}^{2/3}$, which is shown in (2.9). However, when $\beta > 0$, the variation of $\kappa(\beta)$ leads to the modification of Bretherton's result. In what follows, we elucidate this effect by studying the variation of $\kappa(\beta)$ in the limit of small and large values of the van der Waals interaction parameter, β . Since the front and rear menisci of the bubble possess the same curvature, $\kappa(\beta)$, it is sufficient to analyse the front meniscus.

2.3.1. Small β behavior

In this section, we show that when β is small, the thin film profile, H_s , is linearised about Bretherton's $\beta = 0$ profile. In the limit of $\beta \rightarrow 0$, we expand $H_s(X) \sim H_0(X) + \beta H_1(X) + \mathcal{O}(\beta^2)$. Substituting the perturbation expansion into the governing equation (2.12), we

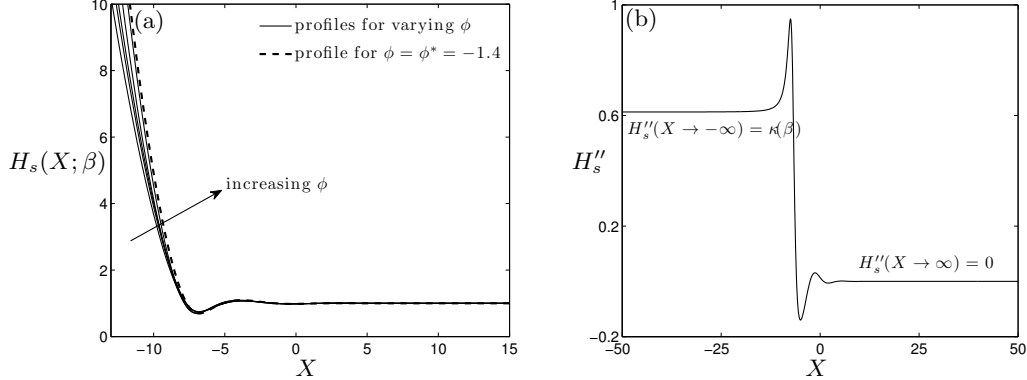


Figure 4: (a) Family of steady-state profiles for the rear meniscus of the bubble for the case of $\beta = 0.2$, and varying phase angle $-1.9 \leq \phi \leq -1.4$. The profile of the rear bubble meniscus which has the same curvature as the front meniscus is shown in the dashed line, where $\phi = \phi^* \approx -1.4$ and $H''_s|_{\text{rear}} = H''_s|_{\text{front}} = \kappa(\beta)$. (b) Variation in the curvature of the rear meniscus profile as a function of position for $\beta = 0.2$ and $\phi = \phi^* \approx -1.4$. The curvature of the rear meniscus equals that of the front meniscus, $\kappa(0.2) \approx 0.611$.

obtain for the first two orders,

$$H_0''' = \frac{H_0 - 1}{H_0^3}, \quad (2.17a)$$

$$H_1''' + \left(\frac{2 - 3H_0}{H_0^3} \right) H_1 = -\frac{H_0'}{H_0^4}. \quad (2.17b)$$

The leading-order equation (2.17a) is Bretherton's original equation, widely known as the Landau–Levich equation (Landau & Levich 1942).

The profiles of H_0 and H_1 are obtained by solving (2.17a) and (2.17b) numerically, subject to far-field conditions

$$H_0(X) \sim 1 + \eta_0 e^X, \quad H_1(X) \rightarrow 0 \quad \text{as } X \rightarrow -\infty. \quad (2.18)$$

The numerical profiles for the curvatures H_0'' and H_1'' are shown in Fig. 5(a), which indicates the convergence of H_0'' and H_1'' to approximately $\kappa_0 = 0.643$ and $\kappa_1 = -0.169$ respectively as $X \rightarrow +\infty$. Therefore, the curvature at the front meniscus of the bubble is given asymptotically by

$$\kappa(\beta) = \lim_{X \rightarrow \infty} H''_s(X; \beta)|_{\text{front}} \sim \kappa_0 + \kappa_1 \beta \quad \text{as } \beta \rightarrow 0. \quad (2.19)$$

Comparisons between numerical and asymptotic values of the curvature for small values of β are shown in Fig. 3.

2.3.2. Large β behavior

Now we turn our attention to the limiting behavior of $\kappa(\beta)$ as $\beta \rightarrow \infty$. To re-incorporate the spatial variation as $\beta \rightarrow \infty$ we introduce the stretched coordinate, $\tilde{X} = X/\beta$, with $H_s(X; \beta) = H_{\text{out}}(\tilde{X})$. The governing equation (2.12) then becomes

$$\frac{1}{\beta^3} H_{\text{out}}^3 H_{\text{out}}''' + \frac{H_{\text{out}}'}{H_{\text{out}}} + 1 - H_{\text{out}} = 0, \quad (2.20)$$

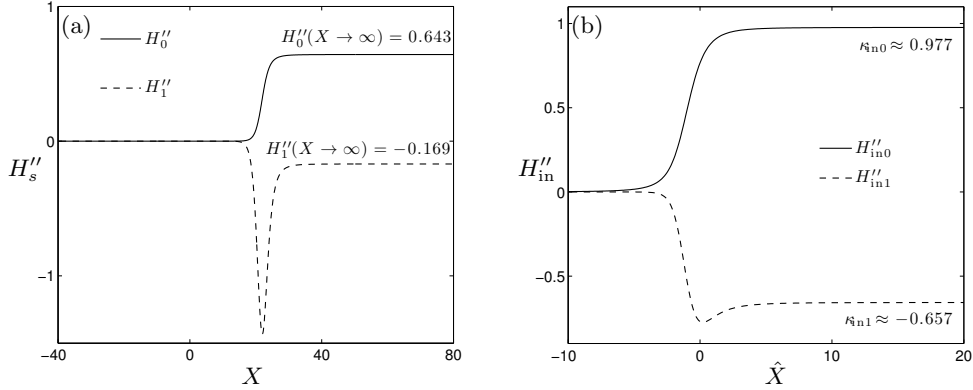


Figure 5: (a) Numerical profiles of the leading-order curvature (H_0'' , solid), and first correction (H_1'' , dashed) for the limit $\beta \rightarrow 0$, as obtained by solving (2.17). (b) Numerical profiles of the leading-order curvature (H_{in0}'' , solid) and first-order curvature (H_{in1}'' , dashed) in the inner region for the limit $\beta \rightarrow \infty$, obtained by solving (2.23).

with primes now denoting derivatives with respect to \hat{X} .

At leading order, we neglect the first term of (2.20) and integrate the result, obtaining

$$H_{out}(\tilde{X}) \sim \frac{1}{1 - e^{(\tilde{X} - \tilde{X}_0)}}, \quad (2.21)$$

where the integration constant \tilde{X}_0 corresponds to an arbitrary translation in \tilde{X} . We shall refer to (2.21) as the ‘outer’ solution, which automatically satisfies the far-field condition $H_{out} \rightarrow 1$ as $\tilde{X} \rightarrow -\infty$. However, the asymptotic solution (2.21) predicts blow-up of the film thickness, with $H_{out}(\tilde{X}) \rightarrow \infty$ as $\tilde{X} \rightarrow \tilde{X}_0$. We therefore seek a boundary layer near the transition point, $\tilde{X} = \tilde{X}_0$, in which the dominant balance in the equation (2.20) changes and incorporates the surface tension term.

We refer to the solution near $\tilde{X} = \tilde{X}_0$ as the ‘inner’ solution. Here, we perform the scalings $\tilde{X} = \tilde{X}_0 + \beta^{-1/2} \hat{X}$ and $H_{out}(\tilde{X}) = \beta^{1/2} H_{in}(\hat{X})$, which transform equation (2.20) into

$$H_{in}^3 H_{in}''' + \frac{H_{in}'}{H_{in}} - H_{in} = -\frac{1}{\sqrt{\beta}}, \quad (2.22)$$

with primes now denoting differentiation with respect to \hat{X} .

Now, we express the inner solution as an asymptotic expansion of the form $H_{in}(\hat{X}) \sim H_{in0}(\hat{X}) + \beta^{-1/2} H_{in1}(\hat{X}) + \dots$ as $\beta \rightarrow \infty$. The leading- and first-order solutions satisfy the differential equations

$$H_{in0}^3 H_{in0}''' + \frac{H_{in0}'}{H_{in0}} - H_{in0} = 0, \quad (2.23a)$$

$$H_{in0}^3 H_{in1}''' + \frac{H_{in1}'}{H_{in0}} + \left(2 - \frac{4H_{in0}'}{H_{in0}^2}\right) H_{in1} = -1, \quad (2.23b)$$

while matching with the outer solution (2.21) leads to the far-field conditions

$$H_{in0}(\hat{X}) \sim -\frac{1}{\hat{X}} + \frac{6}{5\hat{X}^7} + \dots, \quad H_{in1}(\hat{X}) \sim \frac{1}{2} - \frac{3}{\hat{X}^6} + \dots, \quad \text{as } \hat{X} \rightarrow -\infty. \quad (2.24)$$

The inner solutions, H_{in0} and H_{in1} , are numerically computed by solving (2.23) as an

initial-value problem subject to the far-field conditions (2.24) applied at large negative \hat{X} . Then, the differential equations (2.23) are integrated numerically to a large positive value of \hat{X} such that the curvatures, $H''_{\text{in}0}(\hat{X})$ and $H''_{\text{in}1}(\hat{X})$, reach constant values $\kappa_{\text{in}0}$ and $\kappa_{\text{in}1}$ up to numerical error, as illustrated in Fig. 5(b). Hence, the large- β asymptotic behavior of the function $\kappa(\beta)$ is found to be given by

$$\kappa(\beta) \sim \frac{\kappa_{\text{in}0}}{\beta^{1/2}} + \frac{\kappa_{\text{in}1}}{\beta} + \dots \quad \text{as } \beta \rightarrow \infty, \quad (2.25)$$

where $\kappa_{\text{in}0} \approx 0.977$ and $\kappa_{\text{in}1} \approx -0.657$. The asymptotic results (2.19) and (2.25) are displayed as dashed lines in Fig. 3, and are in excellent agreement with the numerical solution of the original differential equation (2.12).

2.3.3. Modified Bretherton relation

In Bretherton's work, corresponding to $\beta = 0$, the normalised film thickness, h_∞/R , scales with $\text{Ca}^{2/3}$. Our generalised relation (2.11) depends implicitly on both h_∞/R and Ca through the van der Waals parameter β , defined by equation (2.8). To unravel the dependence of the deposited film thickness on the capillary number, it is helpful to define an additional dimensionless parameter

$$\delta = \left(\frac{A}{2\pi\gamma R^2} \right)^{1/2}, \quad (2.26)$$

which depends only on the physical properties of the fluid and the tube radius, R . Typical values of the Hamaker constant, A , are in the range 10^{-20} – 10^{-19} J, the interfacial tension, γ , has an order of magnitude of about 10^{-2} J/m², and R may be from a few to a few hundred microns. Therefore, δ is typically small, taking values in the range 10^{-6} – 10^{-3} .

Now, we can use equations (2.8) and (2.11) to express both h_∞/R and Ca as functions of δ and β , namely

$$\delta^{-1}\text{Ca} = \frac{1}{\beta^{1/2}\kappa(\beta)}, \quad \delta^{-2/3} \left(\frac{h_\infty}{R} \right) = \left(\frac{\kappa(\beta)}{\beta} \right)^{1/3}. \quad (2.27)$$

As β ranges between 0 and ∞ , the equations (2.27) parametrically define a functional relationship between $\delta^{-2/3}h_\infty/R$ and $\delta^{-1}\text{Ca}$, which is plotted as a solid curve in Fig. 6. This indicates that the film thickness, h_∞ , is an increasing function of the capillary number, as expected. The detailed behavior may be clarified by using the asymptotic approximations obtained above.

First, considering the limit $\beta \rightarrow 0$, equation (2.19) shows that $\kappa(\beta)$ approaches the constant value $\kappa(0) = \kappa_0 \approx 0.643$. Equation (2.27) therefore reduces to

$$\text{Ca} \sim \frac{\delta}{\kappa_0\beta^{1/2}}, \quad \frac{h_\infty}{\delta^{2/3}R} \sim \frac{\kappa_0^{1/3}}{\beta^{1/3}} \sim \kappa_0 \left(\frac{\text{Ca}}{\delta} \right)^{2/3} \quad \text{for } \beta \ll 1. \quad (2.28)$$

In the limit of large β , the asymptotic expansion (2.25) of $\kappa(\beta)$ reduces (2.27) to

$$\frac{\text{Ca}}{\delta} \sim \frac{1}{\kappa_{\text{in}0}} + \frac{|\kappa_{\text{in}1}|}{\kappa_{\text{in}0}^2} \beta^{-1/2}, \quad \frac{h_\infty}{\delta^{2/3}R} \sim \kappa_{\text{in}0}^{1/3} \beta^{-1/2} \quad \text{for } \beta \gg 1, \quad (2.29)$$

which may be rearranged to

$$\frac{h_\infty}{\delta^{2/3}R} \sim \frac{\kappa_{\text{in}0}^{7/3}}{|\kappa_{\text{in}1}|} \left(\frac{\text{Ca}}{\delta} - \frac{1}{\kappa_{\text{in}0}} \right) \approx 1.442 \left(\frac{\text{Ca}}{\delta} - 1.024 \right). \quad (2.30)$$

The dashed curves in Fig. 6 verify that the approximate relations (2.28) and (2.30) are approached in the relevant limits.

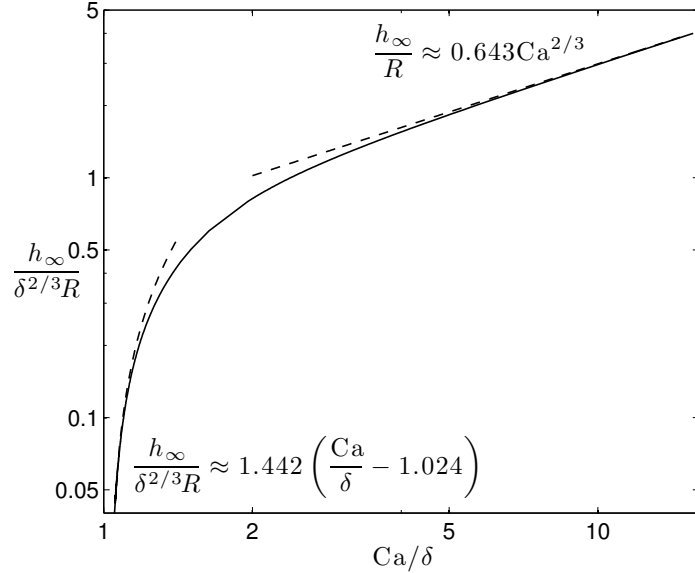


Figure 6: The relation between the normalised film thickness, $\delta^{-2/3}h_\infty/R$, and the scaled capillary number, $\delta^{-1}\text{Ca}$, given parametrically by (2.27). The dashed curves show the asymptotic limits (2.28) as $\beta \rightarrow 0$ and (2.30) as $\beta \rightarrow \infty$.

Now we can interpret the results as follows:

(a) Bretherton's result (2.9) is recovered when β is small, which corresponds to the capillary number being sufficiently large, namely

$$\delta \ll \text{Ca} \ll 1. \quad (2.31)$$

(b) The relation between h_∞/R and Ca starts to depart significantly from Bretherton's prediction when $\text{Ca} = \mathcal{O}(\delta)$.

(c) The film thickness, h_∞ , left behind by the front meniscus reaches zero at a finite critical value of the capillary number,

$$\text{Ca}_{\text{crit}} \approx 1.024 \delta. \quad (2.32)$$

For capillary numbers smaller than this value, no steady film will be left behind the advancing front meniscus.

3. Unsteady solutions

3.1. motivation

So far, we have shown that, for a bubble moving in a tube, and subject to attractive van der Waals forces, steady-state free-surface profiles exist for $\beta > 0$. In this section, we study time-dependent solutions of a thin film for a translating bubble in the presence of attractive intermolecular forces. First, we perform a linear stability analysis to determine the conditions under which a steady-state profile can persist without being destabilised by van der Waals effects. Second, we compute numerical solutions inspired by the experimental configuration of Chen *et al.* (2013), who studied the adhesion of oil drops in a tube filled with water where the surface chemistry of the tube was changed in such a way that part of

it was hydrophilic and another part hydrophobic. Chen *et al.* (2013) found that whether the drops adhere to the tube wall depends both on the capillary number and on the drop length L . When the capillary number is increased beyond a critical value, adhesion to the wall is suppressed; moreover, the critical capillary number is an increasing function of L [*c.f.* Fig. 3 of Chen *et al.* (2013)].

The capillary numbers used in Chen *et al.*'s experiments are of order 10^{-4} – 10^{-3} , while the dimensionless parameter δ is of order 10^{-6} . Therefore the experiments are in the parameter regime $\delta \ll \text{Ca} \ll 1$, corresponding to $0 < \beta \ll 1$. We will use this fact to construct an asymptotic estimate for the time taken for the thin liquid film to rupture (Secs. 3.3–3.5). By comparing this rupture time with the transit time L/U from the front to the rear of the bubble, we predict the dependence of the critical capillary number on the bubble length (Sec. 3.6).

3.2. Linear stability

We first study the stability of the time-dependent equation (2.7) using a normal mode analysis. Perturbing the base state of the uniform film thickness, we set

$$H(X, T; \beta) = 1 + \epsilon e^{ikX + \sigma T}, \quad (3.1)$$

and linearise for infinitesimal perturbations in the limit $\epsilon \ll 1$. Thus, we obtain the dispersion relation

$$\sigma = -k^4 + \beta k^2 + ik \quad (3.2)$$

between the linear growth rate σ and the wave number k . This result is essentially the same as the dispersion relation obtained for a stationary film subject to viscous, surface tension, and van der Waals forces except for a travelling wave term, ik . By analogy, the result is similar to that obtained by Davis *et al.* (2010) for a thin film subject to shear forces. Note that linear stability predicts, according to (3.2), that the film is stable for $\beta \leq 0$, and unstable to long-wave perturbations for any $\beta > 0$.

From (3.2), we find that the most rapidly growing mode, i.e. the wavenumber k_c that maximises $\Re(\sigma)$, corresponds to a wavelength and growth rate given by

$$\lambda_c = \frac{2\pi}{k_c} = 2\pi\sqrt{\frac{2}{\beta}}, \quad \Re(\sigma_c) = -k_c^4 + \beta k_c^2 = \frac{\beta^2}{4}, \quad (3.3)$$

respectively. We conclude that wavelengths of order $\beta^{-1/2}$ or longer are expected to be unstable, and that a characteristic time for the instability to occur should be proportional to β^{-2} .

3.3. Switching on disjoining pressure

To model the experimental set-up of Chen *et al.* (2013), we now consider a situation where the destabilising disjoining pressure is only present in one section of a tube (Fig. 7). The dimensional governing equation (2.5) is thus modified to

$$\frac{\partial h}{\partial t} + \frac{1}{3\mu} \frac{\partial}{\partial x} \left[\gamma h^3 \frac{\partial^3 h}{\partial x^3} + \frac{A\mathcal{H}(x + Ut)}{2\pi h} \frac{\partial h}{\partial x} - 3\mu Uh \right] = 0, \quad (3.4)$$

where \mathcal{H} is the Heaviside step function, so that the term proportional to A switches on across $x = -Ut$ (in our reference frame that moves with the advancing bubble).

When t is negative, before the front meniscus has reached $x = -Ut$, there is no disjoining pressure effect and the problem reduces to Bretherton's model. In this case, the film thickness is given by equation (2.9), and we now use this thickness specifically when

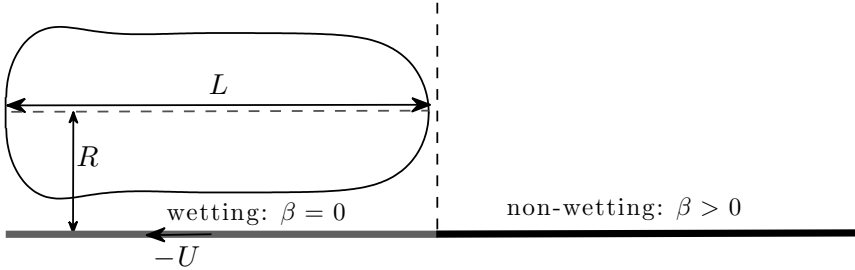


Figure 7: Schematic showing the section of a tube where the disjoining pressure is switched on. The bubble translates across a section of the surface where the wetting state changes (from wetting to non-wetting). This is modelled as a step transition in the thin-film equation (3.4).

non-dimensionalising (3.4). With h_∞ replaced by Bretherton's value (2.9), the definition (2.8) of β is replaced by a new dimensionless parameter

$$\alpha = \frac{A}{2\pi\gamma R^2\kappa_0^2\text{Ca}^2} = \frac{\delta^2}{\kappa_0^2\text{Ca}^2}, \quad (3.5)$$

where δ is still defined by equation (2.26). We also use the results (3.3) of the linear stability analysis to select an appropriate time-scale over which the disturbances to the uniform thin film are expected to grow. These ideas motivate the following choice of new dimensionless variables:

$$\eta = \frac{h}{\kappa_0 R \text{Ca}^{2/3}}, \quad \xi = \frac{x}{\kappa_0 R \text{Ca}^{1/3}}, \quad \tau = \frac{t}{\alpha^{-2} \kappa_0^5 R \text{Ca}^{1/3} / U}, \quad (3.6)$$

and the governing equation (3.4) then becomes

$$\alpha^2 \frac{\partial \eta}{\partial \tau} + \frac{\partial}{\partial \xi} \left[\eta^3 \frac{\partial^3 \eta}{\partial \xi^3} + \alpha \frac{\mathcal{H}(\tau + \alpha^2 \xi)}{\eta} \frac{\partial \eta}{\partial \xi} - \eta \right] = 0. \quad (3.7)$$

The boundary conditions relevant to the front meniscus are

$$\eta \rightarrow \eta_\infty \quad \text{as } \xi \rightarrow -\infty, \quad \frac{\partial^2 \eta}{\partial \xi^2} \rightarrow \kappa_0 \quad \text{as } \xi \rightarrow +\infty, \quad (3.8)$$

where η_∞ is the normalised thickness of the deposited liquid film.

With the parameter values corresponding to the experiments of Chen *et al.* (2013), α is small, of order 10^{-4} or less. When terms of order α^2 are neglected, equation (3.7) becomes quasi-steady. For $\tau < 0$, we retrieve Bretherton's problem, for which we know that a uniform film of unit dimensionless thickness will be deposited, i.e. $\eta_\infty = 1$. For $\tau > 0$, the disjoining pressure term switches on, and for $\beta \ll 1$ the resulting deposited film thickness may be inferred from the results of Sec. 2.3.3,

$$\eta_\infty = \frac{\kappa(\beta)}{\kappa_0} \sim 1 - \frac{|\kappa_1|}{\kappa_0} \alpha, \quad (3.9)$$

when the smallness of α is exploited. Thus, the thickness of the film deposited behind the front meniscus decreases by a small factor of order α as τ increases through zero.

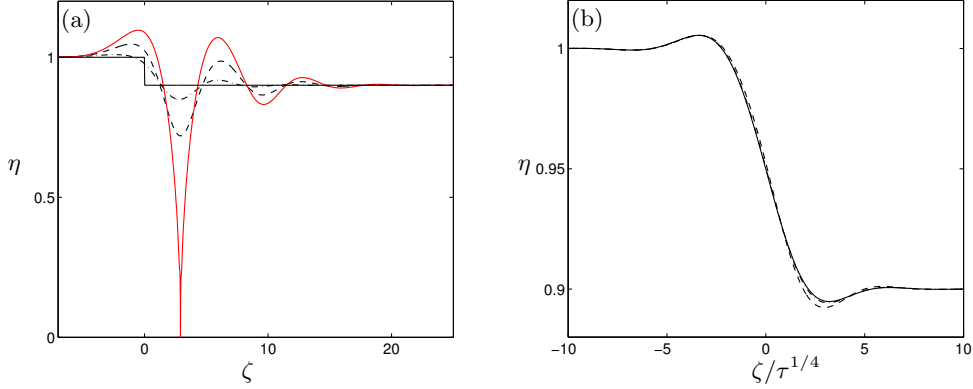


Figure 8: (a) The numerical solution $\eta(\zeta, \tau)$ of the problem (3.11)–(3.12) with $\nu = 0.1$ and $\tau = 0, 3, 6, 7.2404$. (b) The solution plotted versus the similarity variable $\zeta/\tau^{1/4}$ for $\tau = 0.001, 0.01, 0.1$; the dashed curve shows the similarity solution (3.14).

3.4. Numerical solution

To follow the progress of the instability, we shift to a frame that moves with the tube wall by using the travelling-wave coordinate

$$\zeta = \alpha^{1/2} (\xi + \alpha^{-2} \tau). \quad (3.10)$$

This transforms equation (3.7) to

$$\frac{\partial \eta}{\partial \tau} + \frac{\partial}{\partial \zeta} \left[\eta^3 \frac{\partial^3 \eta}{\partial \zeta^3} + \frac{\mathcal{H}(\zeta)}{\eta} \frac{\partial \eta}{\partial \zeta} \right] = 0, \quad (3.11)$$

while matching with the quasi-static front meniscus implies the boundary and initial conditions

$$\eta \rightarrow 1 \quad \text{as } \zeta \rightarrow -\infty, \quad (3.12a)$$

$$\eta \rightarrow 1 - \nu \quad \text{as } \zeta \rightarrow +\infty, \quad (3.12b)$$

$$\eta = 1 - \nu \mathcal{H}(\zeta) \quad \text{at } \tau = 0, \quad (3.12c)$$

where we have introduced the shorthand

$$\nu = \frac{|\kappa_1|}{\kappa_0} \alpha = \frac{|\kappa_1|}{\kappa_0^3} \frac{\delta^2}{\text{Ca}^2} \approx 0.636 \frac{\delta^2}{\text{Ca}^2}. \quad (3.13)$$

For each given value of ν , we solve the problem (3.11)–(3.12) numerically using the method of lines. A sample solution is shown in Fig. 8(a), with $\nu = 0.1$. The discontinuous initial condition is instantaneously smoothed out, as illustrated in Fig. 8(b), where we show that $\eta(\zeta, \tau)$ approaches the similarity solution

$$\eta(\zeta, \tau) \sim 1 - \nu f \left(\zeta/\tau^{1/4} \right) \quad \text{as } \tau \rightarrow 0, \quad (3.14a)$$

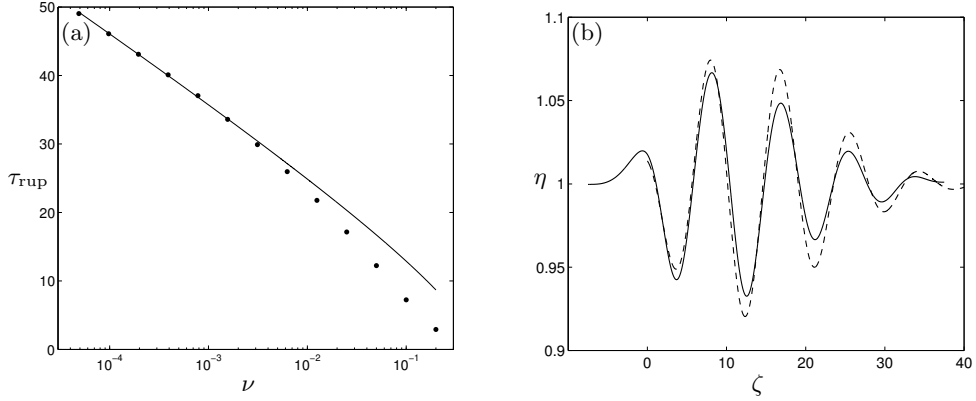


Figure 9: (a) Normalised rupture time τ_{rup} versus scaled van der Waals parameter ν . The dots show the results obtained from numerical solutions of (3.11)–(3.12); the solid curve shows the asymptotic prediction (3.20) with $C = 0.3$. (b) Numerical solution of (3.11)–(3.12) with $\nu = 0.0001$ and $\tau = 40$; the dashed curve shows the large- τ asymptotic solution $1 - \nu\eta_1$, with η_1 given by equation (3.18).

with

$$f(z) = \frac{1}{2} + \frac{\Gamma(5/4)z}{\pi} {}_1F_3\left(\frac{1}{4}; \frac{1}{2}, \frac{3}{4}, \frac{5}{4}; \frac{z^4}{256}\right) + \frac{\Gamma(-1/4)z^3}{96\pi} {}_1F_3\left(\frac{3}{4}; \frac{5}{4}, \frac{3}{2}, \frac{7}{4}; \frac{z^4}{256}\right), \quad (3.14b)$$

where Γ and ${}_1F_3$ denote, respectively, the Gamma function and the generalised hypergeometric function. This solution corresponds to related problems of capillary levelling of a thin film (Salez *et al.* 2012); a related similarity solution arises in studies of the deformation of an elastica in a viscous fluid (Stone & Duprat 2015). In Fig. 8(a), as τ increases further, the instability starts to take effect in $\zeta > 0$, where the disjoining pressure term is present, and ultimately results in rupture.

3.5. Asymptotic rupture time

As the value of ν is decreased, the rupture time τ_{rup} increases, as shown by the numerical results summarised in Fig. 9(a). To examine the limiting behavior as $\nu \rightarrow 0$, we expand the film thickness in the form

$$\eta \sim 1 - \nu\eta_1 + \dots \quad (3.15)$$

Expanding the problem (3.11)–(3.12) for small ν , we find that η_1 satisfies the linear PDE

$$\frac{\partial\eta_1}{\partial\tau} + \frac{\partial^4\eta_1}{\partial\zeta^4} + \frac{\partial}{\partial\zeta}\left[\mathcal{H}(\zeta)\frac{\partial\eta_1}{\partial\zeta}\right] = 0, \quad (3.16)$$

along with the boundary and initial conditions

$$\eta_1 \rightarrow 0 \quad \text{as } \zeta \rightarrow -\infty, \quad (3.17a)$$

$$\eta_1 \rightarrow 1 \quad \text{as } \zeta \rightarrow +\infty, \quad (3.17b)$$

$$\eta_1 = \mathcal{H}(\zeta) \quad \text{at } \tau = 0. \quad (3.17c)$$

The solution $\eta_1(\zeta, \tau)$ may be found by taking a Laplace transform in τ . The resulting inversion integral is unwieldy but may be analysed in the limit of large τ by using the method of steepest descent. A lengthy calculation leads to the following asymptotic approximation for the solution when $\zeta > 0$ and $\tau \gg 1$:

$$\eta_1(\zeta, \tau) \sim 1 + \frac{1}{\sqrt{\pi} \tau^{3/2}} \exp\left(\frac{\tau}{4} - \frac{\zeta^2}{8\tau}\right) \left[(4 + \zeta) \sin\left(\frac{\zeta}{\sqrt{2}}\right) - \sqrt{2}(2 + \zeta) \cos\left(\frac{\zeta}{\sqrt{2}}\right) \right]. \quad (3.18)$$

In Fig. 9(b) we illustrate the accuracy of this approximation by plotting the numerical solution of (3.11)–(3.12) for $\eta(\zeta, \tau)$ with $\nu = 0.0001$ and $\tau = 40$ (solid curve) along with the approximation (3.18).

Equation (3.18) implies that the maximum value of η_1 occurs when $\zeta \sim 2\tau^{-1/2}$ and is given approximately by

$$\eta_{1\max}(\tau) \sim 2\sqrt{\frac{3}{\pi e}} \frac{e^{\tau/4}}{\tau} \quad \text{as } \tau \rightarrow \infty. \quad (3.19)$$

When τ is so large that the perturbation η_1 becomes of order $1/\nu$, the asymptotic ansatz (3.15) ceases to be valid, and one must resort to numerical solution of the full governing equation (3.11). However, we can anticipate that the subsequent nonlinear evolution and rupture takes place over an $\mathcal{O}(1)$ time-scale. We can therefore invert equation (3.19) to obtain an estimate for the normalised time τ_{rup} taken for the film to rupture, namely

$$\tau_{\text{rup}} \sim 4 \log(1/\nu) + 4 \log \log(1/\nu) + C, \quad (3.20)$$

where C is an $\mathcal{O}(1)$ constant. The solid curve in Fig. 9(a) demonstrates that equation (3.20) provides a very good fit for the behaviour of τ_{rup} as $\nu \rightarrow 0$, with $C \approx 0.3$.

3.6. Prediction of the critical capillary number

By reversing the non-dimensionalisation (3.6), we infer from (3.20) the corresponding dimensional rupture time, namely

$$t_{\text{rup}} = \frac{\kappa_0^5 R \text{Ca}^{1/3}}{\alpha^2 U} \tau_{\text{rup}} = \frac{\kappa_0^9 R \text{Ca}^{13/3}}{\delta^4 U} \tau_{\text{rup}}. \quad (3.21)$$

If t_{rup} is greater than the transit time L/U , then the free-surface disturbance will be swept up by the rear meniscus before rupture has time to occur. Therefore rupture is not expected to occur if the capillary number exceeds a critical value Ca_{crit} , which is found by setting $t_{\text{rup}} = L/U$, i.e.

$$\frac{L}{R} = \frac{\kappa_0^9 \text{Ca}_{\text{crit}}^{13/3}}{\delta^4} \tau_{\text{rup}} \approx 0.15 \frac{\text{Ca}_{\text{crit}}^{13/3}}{\delta^4} \log\left(\frac{\text{Ca}_{\text{crit}}}{\delta}\right). \quad (3.22)$$

The result in Eq. (3.22) indicates that the critical capillary number beyond which rupture is suppressed increases with increasing bubble length. This is qualitatively consistent with the experimental results of Chen *et al.*, however, it is not quantitatively consistent. Chen *et al.* found that the critical capillary number varies approximately with $L^{3/4}$ [*c.f.* Fig. 3 of Chen *et al.* (2013)], which does not agree with either our numerical or asymptotic models. We note that the large scatter in the experimental data, and the fact that they studied oil droplets not significantly longer than the tube radius ($L \approx R - 6R$), could be the main reason behind this quantitative disagreement.

4. Discussion

In this paper, we considered the unsteady motion of an inviscid bubble advancing at a constant speed in a cylindrical capillary tube, and subject to destabilising van der Waals forces. Analytical expressions for the steady-state film profile, $H_s(X; \beta)$, depending on the dimensionless van der Waals parameter, β , were derived in the limiting cases of large and small β . To better understand the experimental results of Chen *et al.* (2013), we analysed how the Bretherton steady-state (when $\beta = 0$) is modified when attractive van der Waals forces become significant through a sudden transition from wetting to non-wetting substrates.

Our asymptotic analysis demonstrates that if the bubble length is sufficiently small, then rupture is not expected to occur [*c.f.* (3.22)]; these calculations are found to be in excellent agreement with numerical simulations of the unsteady problem when the van der Waals coefficient is small [*c.f.* Fig. 9(a)]. However, as discussed in Sec. 3.6, while our asymptotic and numerical models agree qualitatively with the experiments of Chen *et al.* (2013), we were unable to produce strong evidence of quantitative agreement. It is unclear whether this is due to scatter in the experimental error, or due to differing assumptions of our models. We highlight the need to develop a full numerical and analytical model which would allow for arbitrary bubble lengths (and thus more complex interaction between the front and rear menisci), and this is the subject of ongoing work.

In the instances that rupture cannot be completely suppressed through modification of the flow velocity, there are other ways to delay its onset. For example, Matar & Kumar (2004) showed that the addition of surfactants causes an increase in the time it takes for a thin film to rupture. The effect of the surfactant is accompanied by a higher capillary number and a thicker deposited film, which may in turn suppress rupture. In their study, Matar & Kumar (2004) also showed that substrate flexibility has an effect on delaying rupture; given the particular importance and desirability of rupture in certain industrial applications (*e.g.* drug delivery [Arap *et al.* (1998)]), we highlight the importance of developing a better understanding of the dynamics of bubbles or drops in non-wetting flexible tubes. Moreover, the delay of rupture due to substrate flexibility sheds light on how the underlying substrate geometry can play a role in delaying or suppressing rupture. Several studies have sought to understand the dynamics of thin-film flow on general curved surfaces (Schwartz & Weidner 1995; Jensen 1997; Howell 2003) and for example, the recent work of Trinh *et al.* (2014) had demonstrated that substrate curvature can prevent the classical Rayleigh-Taylor instability from occurring. It would be expected that similar considerations can be made for the situation of rupture instabilities.

Acknowledgements: The authors would like to thank Jens Eggers and Isabelle Cantat for helpful conversations. We also gratefully acknowledge the Oxford-Princeton Collaborative Workshop Initiative for providing an opportunity for this collaborative work.

REFERENCES

ARAP, W., PASQUALINI, R. & RUOSLAHTI, E. 1998 Cancer treatment by targeted drug delivery to tumor vasculature in a mouse model. *Science* **279**, 377–380.

BLACKSTONE, B. N., WILLARD, J. J., LEE, C. H., NELSON, M. T., HART, R. T., LANNUTTI, J. J. & POWELL, H. M. 2012 Plasma surface modification of electrospun fibers for adhesion-based cancer cell sorting. *Integr. Biol.* **4**, 1112–1121.

BRETHERTON, F. P. 1960 The motion of long bubbles in tubes. *J. Fluid Mech.* **10**, 166–188.

BURELBACH, J. P., BANKOFF, S. G. & DAVIS, S. H. 1988 Nonlinear stability of evaporating/condensing liquid films. *J. Fluid Mech.* **195**, 463–494.

CHAUDHURY, K., ACHARYA, P. V. & CHAKRABORTY, S. 2014 Influence of disjoining pressure on the dynamics of steadily moving long bubbles inside narrow cylindrical capillaries. *Phys. Rev. E* **89** (053002).

CHEN, H., DONG, E., LI, J. & STONE, H. A. 2013 Adhesion of moving droplets in microchannels. *Appl. Phys. Lett.* **103** (131605).

DAVIS, M. J., GRATTON, M. B. & DAVIS, S. H. 2010 Suppressing van der Waals driven rupture through shear. *J. Fluid Mech.* **661**, 522–539.

ERBIL, H. Y., DEMIREL, A. L., AVCI, Y. & MERT, O. 2003 Transformation of a simple plastic into a superhydrophobic surface. *Science* **299**, 1377–1380.

FAIRBROTHER, F. & STUBBS, A. E. 1935 Studies in electro-endosmosis. Part VI. The “bubble-tube” method of measurement. *J. Chem. Soc.* **1**, 527–529.

GAVER, D. P., HALPERN, D., JENSEN, O. & GROTBORG, J. B. 1996 The steady motion of a semi-infinite bubble through a flexible-walled channel. *J. Fluid Mech.* **319**, 25–65.

GOLDSMITH, H. L. & MASON, S. G. 1963 The flow of suspensions through tubes II. Single large bubbles. *J. Colloid Sci.* **18**, 237–261.

HAMMOUD, N. 2016 Problems in interfacial thin-film instabilities. PhD thesis, Princeton University.

HEIL, M. 1999 Airway closure: occluding liquid bridges in strongly buckled elastic tubes. *J. Biomech. Eng.-T. ASME* **121**, 487–493.

HODGES, S. R., JENSEN, O. E. & RALLISON, J. M. 2004 The motion of a viscous drop through a cylindrical tube. *J. Fluid Mech.* **501**, 279–301.

HOWELL, P. D. 2003 Surface-tension-driven flow on a moving curved surface. *J. Eng. Math.* **45**, 283–308.

IDA, M. P. & MIKSIS, M. J. 1996 Thin film rupture. *Appl. Math. Lett.* **9** (3), 35–40.

JENSEN, O. E. 1997 The thin liquid lining of a weakly curved cylindrical tube. *J. Fluid Mech.* **331**, 373–403.

KALPATHY, S. K., FRANCIS, L. F. & KUMAR, S. 2010 Shear-induced suppression of rupture in two-layer thin liquid films. *J. Colloid Interface Sci.* **348**, 271–279.

KOCH, K., BHUSHAN, B., JUNG, Y. C. & BARTHLOTT, W. 2009 Fabrication of artificial lotus leaves and significance of hierarchical structure for superhydrophobicity and low adhesion. *Soft Matter* **5**, 1386–1393.

LANDAU, L. & LEVICH, B. 1942 Dragging of a liquid by a moving plate. *Acta Physicochim. URSS.* **17**, 42–54.

MATAR, O. K. & KUMAR, S. 2004 Rupture of a surfactant-covered thin liquid film on a flexible wall. *SIAM J. Appl. Math.* **64**, 2144–2166.

ORON, A., DAVIS, S. H. & BANKOFF, S. G. 1997 Long-scale evolution of thin liquid films. *Rev. Mod. Phys.* **69**, 931–980.

PARK, C.-W. & HOMSY, G. M. 1984 Two-phase displacement in Hele-Shaw cells: theory. *J. Fluid Mech.* **139**, 291–308.

ROACH, P., SHIRTCLIFFE, N. J. & NEWTON, M. I. 2008 Progress in superhydrophobic surface development. *Soft Matter* **4**, 224–240.

SALEZ, T., MCGRAW, J. D., BÄUMCHEN, O., DALNOKI-VERESS, K. & RAPHAËL, E. 2012 Capillary-driven flow induced by a stepped perturbation atop a viscous film. *Phys. Fluids* **24** (102111).

SCHWARTZ, L. W., PRINCEN, H. M. & KISS, A. D. 1986 On the motion of bubbles in capillary tubes. *J. Fluid Mech.* **172**, 259–275.

SCHWARTZ, L. W. & WEIDNER, D. E. 1995 Modeling of coating flows on curved surfaces. *J. Eng. Math.* **29**, 91–103.

STONE, H. A. & DUPRAT, C. 2015 Model problems coupling elastic boundaries and viscous flows. In *Fluid-Structure Interactions in Low-Reynolds-Numbers Flows* (ed. C. Duprat & H.A. Stone). Royal Society of Chemistry.

TAI, C.-F., BIAN, S., ZHENG, D., HALPERN, Y., FILOCHE, M. & GROTBORG, J. B. 2011 Numerical study of flow fields in an airway closure model. *J. Fluid Mech.* **677**, 483–502.

TAYLOR, G. I. 1961 Deposition of a viscous fluid on the wall of a tube. *J. Fluid Mech.* **10**, 161–165.

TELETZKE, G. F., DAVIS, H. T. & SCRIVEN, L. E. 1988 Wetting hydrodynamics. *Rev. Phys. Appl.* **23**, 989–1007.

TRINH, P. H., KIM, H., HAMMOUD, N., HOWELL, P. D., CHAPMAN, S. J. & STONE, H. A. 2014 Curvature suppresses the Rayleigh-Taylor instability. *Phys. Fluids* **26** (051704).

WILSON, S. D. R. & JONES, A. F. 1983 The entry of a falling film into a pool and the air-entrainment problem. *J. Fluid Mech.* **128**, 219–230.

WITELSKI, T. P. & BERNOFF, A. J. 1999 Stability of self-similar solutions for van der Waals driven thin film rupture. *Phys. Fluids* **11**, 2443–2445.

WITELSKI, T. P. & BERNOFF, A. J. 2000 Dynamics of three-dimensional thin film rupture. *Physica D* **147**, 155–176.

WONG, H., RADKE, C. J. & MORRIS, S. 1995a The motion of long bubbles in polygonal capillaries. Part 1. Thin films. *J. Fluid Mech.* **292**, 71–94.

WONG, H., RADKE, C. J. & MORRIS, S. 1995b The motion of long bubbles in polygonal capillaries. Part 2. Drag, fluid pressure and fluid flow. *J. Fluid Mech.* **292**, 95–110.

ZHANG, W. W. & LISTER, J. R. 1999 Similarity solutions for van der Waals rupture of a thin film on a solid substrate. *Phys. Fluids* **11**, 2454–2462.